

RESEARCH ARTICLE

10.1002/2014JA019975

Key Points:

- Chorus at South Pole is absent at main phase and not enhanced at recovery
- Chorus at Palmer is enhanced during storm main and recovery phases
- Chorus is more intense for storms with rapid outer belt flux increases

Correspondence to:

M. Spasojevic,
mariaspasojevic@stanford.edu

Citation:

Spasojevic, M. (2014), Statistical analysis of ground-based chorus observations during geomagnetic storms, *J. Geophys. Res. Space Physics*, 119, doi:10.1002/2014JA019975.

Received 12 MAR 2014

Accepted 24 SEP 2014

Accepted article online 30 SEP 2014

Statistical analysis of ground-based chorus observations during geomagnetic storms

M. Spasojevic¹¹Department of Electrical Engineering, Stanford University, Stanford, California, USA

Abstract Chorus observations from two ground-based, Antarctic receiving stations are analyzed for a set of geomagnetic storms from 2000 to 2010. Superposed epoch analysis is performed together with statistical hypothesis testing to determine whether the observed quantities (geomagnetic indices, outer belt energetic electron fluxes, and chorus properties) are statistically significantly different as functions of storm phase, storm size, and storm type. Waves generated in the outer dayside magnetosphere and observed on the ground at South Pole Station are suppressed during main phase and are statistically unchanged from random intervals during recovery phase. Waves generated in the inner magnetosphere and observed on the ground at Palmer Station are significantly enhanced during storm main phase and for about 3 days into recovery. During main phase, there are larger enhancements in chorus occurrence, amplitude, and frequency extent as observed at Palmer during larger storms. During recovery phase, there are larger enhancements in chorus occurrence, amplitude, and frequency extent as observed at Palmer during larger storms and during storms where the average rate of electron flux increase, averaged across the outer belt, is higher.

1. Introduction

There have been significant advances in the past decade in understanding which physical processes are important in controlling the dynamics of the Earth's electron radiation belts during solar-driven geomagnetic disturbances (see reviews by *Millan and Thorne* [2007], *Shprits et al.* [2008a, 2008b], and *Millan and Baker* [2012]). What remains to be quantified is where, when, and under what conditions, specific processes are active and to what degree they individually contribute to the overall balance of acceleration and loss. Increasing attention has been paid to the role of whistler mode chorus emissions in accelerating electrons up to MeV energies via cyclotron resonant wave-particle interactions. There is evidence that chorus-driven acceleration plays a major and possibly dominant [*Thorne*, 2010] role in the reformation of the outer belt in the aftermath of geomagnetic storms. However, a significant confounding factor is that wave-particle interactions involving chorus can also result in significant losses due to the scattering of MeV energy electrons into the loss cone [*Lorentzen et al.*, 2001; *Thorne et al.*, 2005]. The balance between electron acceleration and loss is complex as it depends on a number of parameters including the latitudinal extent of the waves, the electron energy, and pitch angle as well as the background plasma density and magnetic field configuration [*Horne et al.*, 2005; *Shprits et al.*, 2006; *Summers et al.*, 2007; *Orlova and Shprits*, 2010].

A hurdle to quantifying the role of chorus has been the dearth of in situ wave observations in previous solar cycles. The Van Allen Probes dual-spacecraft mission [*Mauk et al.*, 2012], launched in 2012, includes an unprecedented suite of high-resolution wave sensors and is beginning to fill this gap, but a large database of storm time wave measurements is not yet available. A number of previous studies of chorus-driven acceleration and loss [e.g., *Horne et al.*, 2005; *Shprits et al.*, 2007; *Li et al.*, 2007; *Varotsou et al.*, 2008; *Albert et al.*, 2009; *Ni et al.*, 2011] rely on wave measurements from the Combined Release and Radiation Effects Satellite (CRRES), but the mission had a relatively short 15 month lifetime and a rather limited wave receiver.

In contrast, there are solar cycle long data records available from ground-based ELF/VLF receivers, particularly low-noise Antarctic observing stations such as Halley Bay [*Smith et al.*, 2010], Palmer Station [*Golden et al.*, 2011], and South Pole Station [*Yan et al.*, 2013]. Ground-based receivers are capable of observing waves of magnetospheric origin, but the data can be significantly harder to interpret due to a myriad of propagation effects. Waves must travel from the magnetospheric source region to low altitude, through the ionosphere, and possibly some distance in the Earth-ionosphere waveguide before being measured at the receiving station (see section 3.6 for a more detailed discussion of propagation effects). Nevertheless, the

long data records available from these stations provide an opportunity to perform statistical analysis over a large number of geomagnetic storms.

Smith et al. [2004a] used an 11 year (1992–2002) database of ELF/VLF observations from Halley Bay ($L = 4.3$) to statistically examine ground-based wave observations during geomagnetic storms. By applying a superposed epoch analysis, they found that there tends to be a depression of ground-based wave power in the chorus band during storm main phase, and this effect is attributed to the disruption of ducted propagation paths to ground (rather than a lack of chorus generation in the source region). However, *MacDonald et al.* [2008] developed a proxy for whistler mode wave growth using in situ plasma measurements and found that conditions for wave growth are suppressed at geosynchronous altitude in the midnight to dawn sector during the main phase of storms. This suggests that the lack of wave observations reported by *Smith et al.* [2004a] may be a result of reduced wave growth in the magnetosphere. Ground-based chorus activity observed at Halley intensifies during recovery phase with a peak in wave power occurring about 6 h after minimum *Dst*. Near 1 kHz, the recovery phase chorus intensities are independent of storm intensity (minimum *Dst* from -50 to -100 nT versus < -100 nT), but larger storms do result in more intense recovery phase chorus at higher frequencies (near 3 kHz). The observation of higher-frequency chorus during intense storms is attributed to the erosion of the plasmopause and the generation of chorus at lower L .

Smith et al. [2004b] extended analysis of the Halley Bay database by examining differences in ground-based chorus in geomagnetic storms with and without poststorm enhancements in the 1.8–3.5 MeV electron flux (events versus nonevents) as observed at geosynchronous orbit. They found that in the lower frequency bands (0.5–1 kHz), recovery phase chorus power is higher during storms that result high poststorm electron fluxes, but at higher frequencies (near 2 kHz) the nonevents are associated with higher chorus intensity particularly in the early recovery phase. The authors conclude that the association of more intense 0.5–1 kHz chorus waves with electron enhancement events is evidence of chorus-driven electron acceleration while the association of 2 kHz chorus waves with nonevents is attributed to a propagation effect.

Here we present a statistical analysis of ground-based chorus observations from two Antarctic receiving stations at low (Palmer Station, $L = 2.4$) and high (South Pole, $L > 9$) invariant latitude during 144 geomagnetic storms from 2000 to 2010. We examine chorus occurrence, amplitude, and frequency extent as a function of storm phase, storm size, and storm type (corotating interaction region (CIR) versus coronal mass ejection (CME) solar wind driving structure) and also examine the relationship between chorus observations and energetic electrons as observed at geosynchronous orbit and at low altitude. Throughout, we perform statistical hypothesis testing to determine whether the observed quantities (*Dst*, *Kp*, energetic electron flux, and chorus properties) are statistically significantly different as a function of storm phase and type. Our work extends the studies of *Smith et al.* [2004a, 2004b] by using data from ground stations with different magnetospheric viewing areas and improves analysis by applying rigorous statistical hypothesis testing. We also develop a new metric to categorize storms based on the rate of electron flux increase during recovery phase.

2. Data Sets

2.1. Ground-Based ELF/VLF

Stanford University has operated broadband ELF/VLF receivers in Antarctica at Palmer Station (invariant latitude $\Lambda = -50^\circ$, $L = 2.4$, MLT = UT $- 4$ h) and at South Pole Station ($\Lambda = -70^\circ$, $L > 9$, MLT = UT $- 3.5$ h) continuously for several decades. The receivers record wave activity incident upon two orthogonal magnetic loop antennas, and the design of the antennas and preamplifier is described by *Harriman* [2010], while the overall system design is similar to that described by *Cohen et al.* [2010]. Full spectrum broadband data are typically recorded in a synoptic fashion, that is, 1 min of data are saved every 15 min. Historically, the high-volume broadband data was recorded on reel-to-reel analog magnetic tapes. However, beginning in 2000 at Palmer Station and 2001 at South Pole, it became feasible to record the data digitally (two channels each with 100 kHz sampling frequency; 0.3–40 kHz bandwidth). In recent years, tremendous increases in the capacity (and low cost) of digital storage media and the increased processing power of modern desktop computers have allowed us to begin large-scale data mining in a manner that was not previously feasible. The entire database of digital ELF/VLF data from Palmer and South Pole (~ 15 TB) now resides on a hard-drive-based server, and automated algorithms have been developed for event detection and classification.

Golden *et al.* [2011] developed an automated algorithm for detecting chorus and hiss emissions in ground-based broadband ELF/VLF data. The algorithm first cleans the data by removing lightning-generated sferics and power line hum. Next, wave events are detected, and a neural network is used to classify the events based on their spectral characteristics. In Golden *et al.* [2011], the algorithm separates discrete rising emissions characteristic of chorus from band-limited noise characteristic of midlatitude or plasmaspheric hiss and rejects other emissions as noise (including whistlers, sferic bursts, sferic slowtails, and tweeks). The algorithm was applied to 10 years of synoptic broadband data from Palmer Station from May 2000 to May 2010. Due to different natural and manmade noise characteristics, a modified version of the automated emission detector was developed and the neural network retrained using South Pole data. At South Pole, chorus and auroral hiss are identified and other emissions (primarily of anthropogenic origin) are rejected as noise. The algorithm was applied to 8 years of South Pole data from January 2001 to December 2008.

The current study uses the database of detected chorus emissions from both Palmer and South Pole. The database consists of the universal time of the chorus event (in 15 min increments) and the power spectral density (averaged over a 10 s segment of data) as a function of frequency. A total of 12,179 chorus events were detected at Palmer from 308,727 available synoptic intervals (4% overall occurrence), and at South Pole 66,103 chorus events were detected from 181,327 available synoptic intervals (36% occurrence).

In order to examine differences in the occurrence of the chorus at the two stations, it is useful to examine the magnetospheric ELF/VLF viewing area of the two stations. In Figure 1a, the solid blue (South Pole) and green (Palmer) lines show the location of the two stations mapped out to the magnetic equatorial plane (noon is at the top) using the T96 geomagnetic field model [Tsyganenko, 1995] under quiet geomagnetic conditions ($P_{\text{dyn}} = 0.5 \text{ nPa}$, $B_z = B_y = 0 \text{ nT}$, $Dst = 0 \text{ nT}$). The dot indicates the location of the stations at 3 h intervals, and the shaded region around each dot indicates the magnetic mapping of a 500 km radius circle in the ionosphere around the station. If the chorus emissions propagate to the ground primarily in a ducted mode, the shaded region is an estimate of the ELF/VLF viewing area of the station. The convergence of magnetic field lines at high latitudes leads to a large viewing area for South Pole in the equatorial plane. In addition for the lower latitude station, work by Golden *et al.* [2010] determined that a significant portion of the chorus emissions observed at Palmer likely originate at higher L , propagate to low altitude in a nonducted mode (inward cross L propagation) and arrive at the ionosphere (within the ionospheric transmission cone) near the latitude of Palmer. Extensive ray tracing determined that the nonducted ELF/VLF viewing area of Palmer may extend to $\sim 5 R_E$ in the equatorial plane as indicated by the dashed black lines in Figure 1a. In addition, since Palmer is located within the dipolar magnetic field region, the ELF/VLF viewing area is not strongly dependent on MLT nor geomagnetic activity while size and shape of the viewing area at South Pole depends strongly on both MLT and geomagnetic activity (discussed further below).

Before examining chorus observations during geomagnetic storms, we first examine the general features of the ground-based chorus databases and contrast the trends between the high- and low-latitude station. The occurrence of chorus at the two stations is strongly dependent on magnetic local time (MLT) with occurrence peaking near 6 MLT for the lower-latitude Palmer Station (Figure 1c) but just before noon at South Pole (Figure 1b). This is consistent with the earliest studies of chorus from ground-based [Pope, 1960] and in situ observations [Tsurutani and Smith, 1977] and is likely related to the drift paths of the energetic source electrons (5–50 keV), which move outward from dawn to noon due to drift shell splitting. In addition, the overall occurrence probability at South Pole is significantly higher with chorus being observed nearly every-day when the station traverses the outer dayside magnetosphere. The high occurrence rate of chorus in the outer dayside magnetosphere has been reported in other recent studies [Li *et al.*, 2009; Spasojevic and Inan, 2010; Bunch *et al.*, 2011]. In addition, waves in the outer dayside magnetosphere tend to have a weaker dependence on geomagnetic activity than other sectors. This can be seen in Figures 1d and 1e, where chorus occurrence at Palmer is strongly dependent of geomagnetic activity, but chorus at South Pole can be observed over a wider range of geomagnetic conditions including extreme quiet. Several factors contribute to high wave occurrence in the outer dayside magnetosphere including drift shell splitting [Min *et al.*, 2010], extended latitudinal regions of homogenous magnetic field near $\sim 6\text{--}8.5 R_E$ [Spasojevic and Inan, 2010; Keika *et al.*, 2012; Katoh and Omura, 2013], and Shabansky orbits within $1\text{--}2 R_E$ of the magnetopause [McCullough *et al.*, 2012]. However, for the highest Kp levels, chorus occurrence at South Pole decreases. The decrease with increasing activity occurs across all local time sectors, and we believe this is related to the fact that during extreme solar wind driving the ELF/VLF viewing area maps either to open magnetic field lines or to field lines that extend to large distances in the flanks of the magnetotail (see further discussion below). When

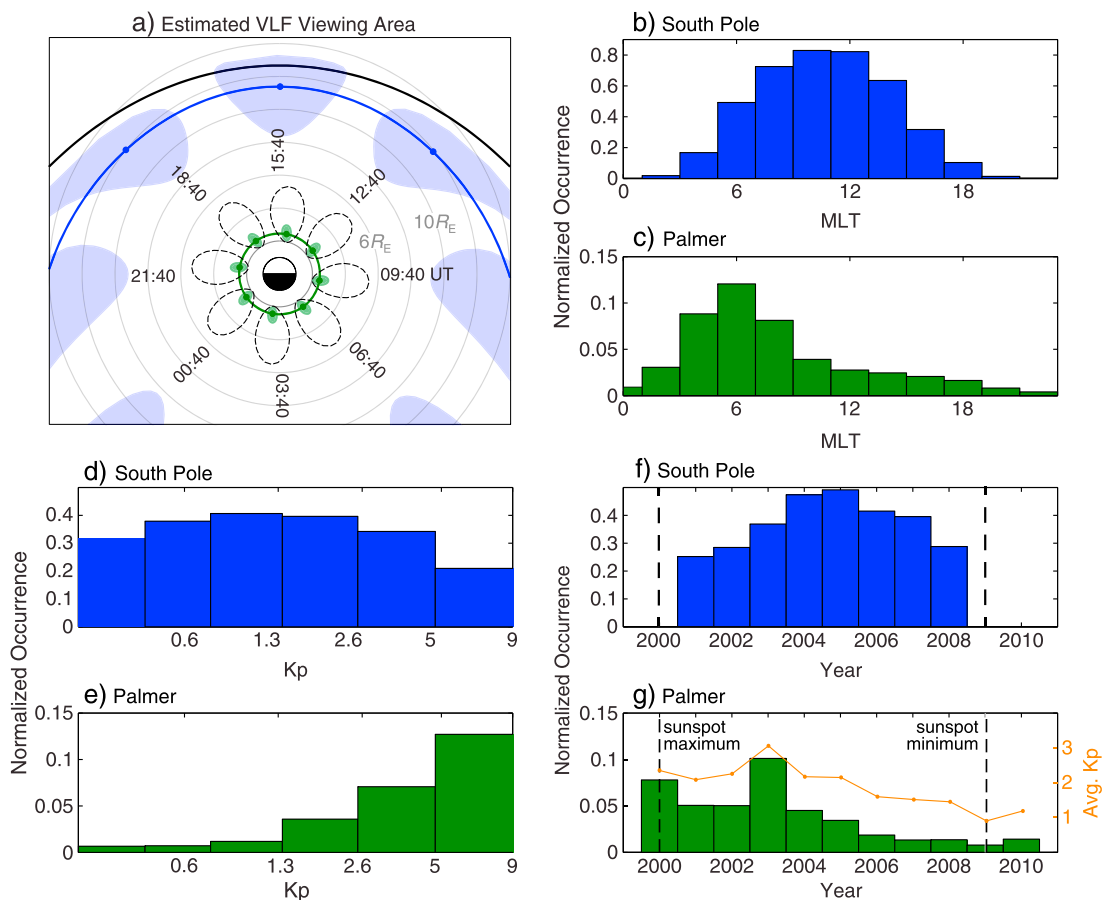


Figure 1. (a) The solid lines show the locations of South Pole (blue) and Palmer (green) stations mapped out to the magnetic equatorial plane over a 24 h interval. The blue and green dots show the mapped location of the stations at the indicated UT. The blue and green-shaded regions around each dot represent the ducted ELF/VLF viewing area of the station taken as the magnetic mapping of a 500 km radius circle in the ionosphere around the station. The black dashed region around the mapped location of Palmer station is an estimate of the nonducted ELF/VLF viewing area of the station. The MLT, K_p , and solar cycle dependence of chorus occurrence observed at (b,d, and f) South Pole and (c,e, and g) Palmer stations. Figure 1g also shows the annual average value of the K_p index in orange.

K_p is in the range of 1–2, chorus occurrence maximizes since the magnetosphere is inflated such that the South Pole viewing area is under closed field lines and there are slightly more source electrons than during the quietest conditions ($K_p < 1$) [e.g., Li *et al.*, 2010b]. In contrast, at Palmer chorus, observations strongly favor highly disturbed geomagnetic conditions. Finally, Figures 1f and 1g show the solar cycle dependence of chorus occurrence, which mimics the K_p dependence with wave occurrence at Palmer favoring the high activity in the peak and declining phase of the solar cycle, but at South Pole, moderate midcycle activity leads to a peak in wave occurrence. Overlaid on Figure 1g is the annual average value of the K_p index, which is well correlated with chorus occurrence at Palmer including the peak in activity seen in 2003.

Next, we explore how the geomagnetic field geometry affects the viewing area of ground-based receiving stations and contributes to the lack of wave activity observed at South Pole under highly disturbed conditions. Figure 2a shows the mapping of the ground stations out to the magnetic equatorial plane under four activity levels using the T96 magnetic field model [Tsyganenko, 1995]. In addition to Palmer and South Pole, we have also included Halley Bay in order to further explore the findings of Smith *et al.* [2004a]. First of all, the magnetic mapping of the low-latitude Palmer station is virtually unaffected by increasing geomagnetic disturbance with all four curves lying on top of one another, and we note that even superstorms, such as the Halloween 2003 storm [Spasojevic and Inan, 2005], are expected to only slightly dilate the viewing area as predicted by the Tsyganenko and Sitnov [2005] model. In contrast, the magnetic mapping of the midlatitude Halley station on the nightside is strongly affected by changing conditions. The magnetic field in the midnight sector becomes highly stretched to $> 14 R_E$ for the “disturbed” (red curve) level, and this may contribute to the lack of chorus during storm main phase reported by Smith *et al.* [2004a] as well as the

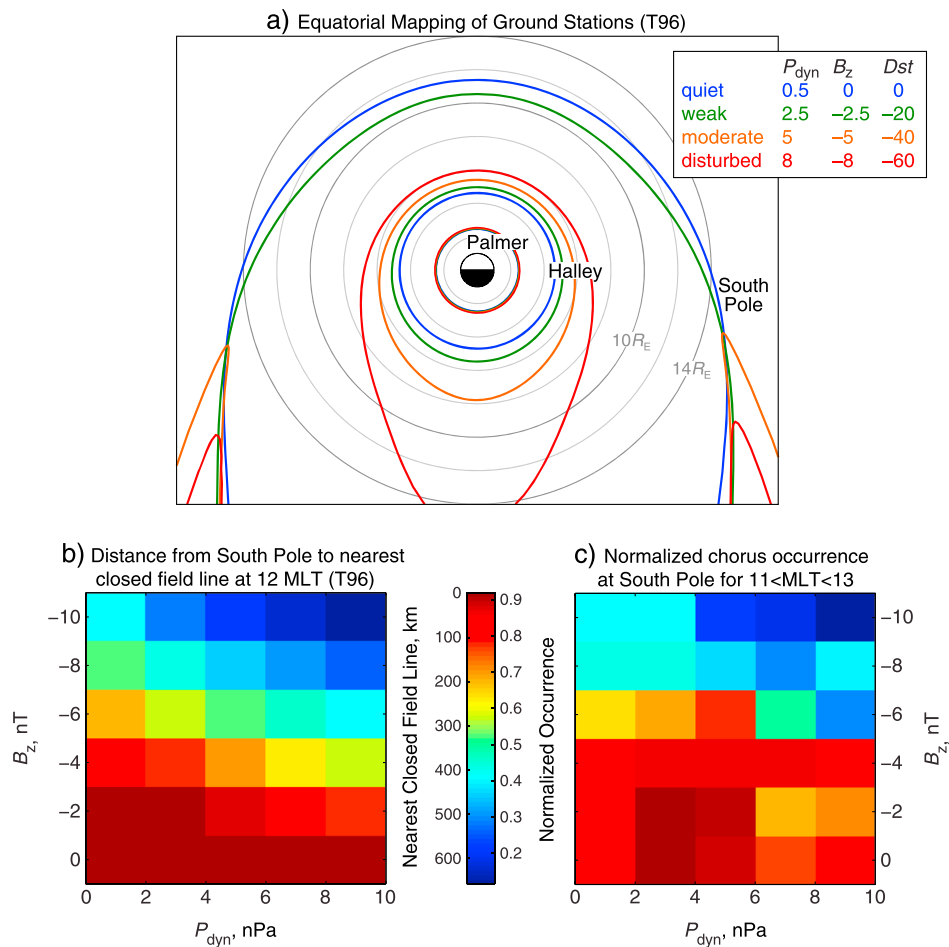


Figure 2. (a) The locations of South Pole, Halley Bay, and Palmer stations mapped out to the magnetic equatorial plane over a 24 h interval for four levels of geomagnetic activity: quiet (blue), weakly disturbed (green), moderately disturbed (orange), and highly disturbed (red) as defined by the values of solar wind dynamic pressure (P_{dyn} in units of nPa), IMF B_z (nT), and Dst (nT) as indicated in the inset. (b) The equatorward distance from South Pole to the nearest closed field line when the station is at 12 MLT as a function of IMF B_z and P_{dyn} . (c) The normalized occurrence of chorus at South Pole for 11 < MLT < 13 as a function of IMF B_z and P_{dyn} .

reduced conditions for whistler mode growth during main phase near midnight at geosynchronous orbit (which would be similarly affected by stretched field geometry) reported by *MacDonald et al.* [2008]. At the high-latitude South Pole station for quiet (blue) and weak (green) disturbance levels, the station maps onto closed field lines inside of $14 R_E$ on the dayside. For the higher activity levels (orange and red), as the station approaches dawn, the field line becomes dragged to great distances down the dawnside flank. Further, when the station reaches $\sim 6-7$ MLT, the field line no longer crosses the equatorial plane and becomes open.

As mentioned previously, the ELF/VLF viewing area of a ground station extends to a region surrounding the exact equatorial mapping since waves can penetrate the ionosphere some distance away from the station and propagate to the station in the Earth-ionosphere waveguide. Figures 2b and 2c show how changing solar wind conditions influence the viewing area of South Pole and chorus observations for the case when the station is at 12 MLT. Figure 2b shows the equatorward distance on the ground from South Pole to the nearest closed magnetic field line as a function of solar wind dynamic pressure (P_{dyn}) and IMF B_z . When B_z is near zero, the field line passing through the station is closed (that is, the distance to the nearest closed field line is 0 km) for all levels of P_{dyn} . Increasing pressure compresses the dayside magnetosphere, but the field line passing through South Pole remains closed. When B_z turns negative, the dayside magnetopause begins to erode [e.g., *Petrinec and Russell*, 1993; *Wiltberger et al.*, 2003] and outer dayside field lines become open. The distance from South Pole to the nearest closed field line then increases for high pressure and

large negative values of B_z . Figure 2c shows the normalized chorus occurrence at South Pole also as a function of P_{dyn} and IMF B_z . For small values of B_z , the occurrence of chorus is high for all values of pressure, but occurrence decreases rapidly for high pressure and large negative B_z (top right corner of Figure 2c). The two-dimensional cross correlation between Figures 2b and 2c is -0.9 , suggesting that the drop in chorus activity at South Pole under disturbed geomagnetic conditions is related to the station being on open field lines and relatively far from closed field lines that map to the chorus source region.

2.2. Geomagnetic Storms and Energetic Particles

A database of geomagnetic storms was compiled for the interval covered by the ground-based chorus measurements, 2000–2010. We start with an updated list of the arrival time at Earth of different types of solar wind structures provided by the authors of Richardson *et al.* [2000, 2002] (including the identification of CME- and CIR-associated structures) and an updated database of solar wind and geomagnetic parameters (including solar wind dynamic pressure P_{dyn} , IMF B_z , Dst , and Kp) at 5 min cadence provided by the authors of Qin *et al.* [2007]. For this study, we choose to identify storms as intervals with a minimum $Dst^* \leq -50$ nT occurring within 1 day of the arrival of either a CME- or CIR-associated solar wind structure. Dst^* is a corrected version of the Dst index that attempts to remove the contribution of magnetopause currents, and we use the Dst^* formulation of O'Brien and McPherron [2000]. Storm onset is defined as the maximum Dst^* between the structure arrival and minimum Dst^* . The storm main phase is then the time from storm onset to minimum Dst^* . The recovery phase begins at minimum Dst^* , and the end of recovery phase is defined as when Dst^* recovers 80% from the minimum value. We further constrain the storm selection such that there are no intervening solar wind structures during the main or recovery phases. Using these criteria, we identified 144 geomagnetic storms from May 2000 to May 2010 (corresponding to the coverage of the Palmer data). Of the 144, 73 storms were driven by CME-associated solar wind structures, and 71 storms were driven by CIR-associated solar wind structures. For the interval from storm onset to the end of storm recovery phase, there are a total of 4163 chorus events observed at Palmer and 7086 chorus events observed at South Pole over all 144 storms.

In order to assess the impact of geomagnetic storms on energetic electron populations, we use the NOAA Space Weather Prediction Center's Daily Particle Data product, which provides a measurement of the daily fluence of electrons for energies >600 keV and >2 MeV at geosynchronous orbit from the Geostationary Operational Environmental Satellites (GOES) [Onsager *et al.*, 1996]. Data from 2000 through 2002 are taken from GOES-8, from 2002 through March 2010 from GOES-11 and after March 2010 from GOES-13, and the daily fluence ($\text{cm}^{-2} \text{day}^{-1} \text{sr}^{-1}$) is converted to daily average flux ($\text{cm}^{-2} \text{s}^{-1} \text{sr}^{-1}$). All analyses were performed on both the >600 keV and >2 MeV data with essentially identical results. Here we present only plots of the >600 keV data since that energy range is more representative of the electron population with which chorus can efficiently resonate [e.g., Orlova *et al.*, 2012]. Although the geosynchronous orbit ($L \approx 6.6$) is somewhat beyond the ELF/VLF viewing area of Palmer, the GOES data is of value since (1) it provides continuous coverage of energetic electrons for all 144 storms and (2) a significant body of research exists on the evolution of the outer belt as observed at geosynchronous, thus providing important context for the current work.

We also analyze energetic electron data from the low-altitude, high-inclination Solar Anomalous and Magnetospheric Particle Explorer (SAMPEX) spacecraft [Baker *et al.*, 1993]. We use daily averages of the electron flux in the 2–6 MeV energy range from the Proton/Electron Telescope (PET). Although the energy range is somewhat higher than typical chorus interactions, the SAMPEX data are valuable as they provide measurements over a broad range of L , allowing for a more global characterization of changes in the outer belt during storms. In this study, we examine two quantities derived from the daily averaged PET data: (1) the 2–6 MeV electron flux averaged over the entire outer belt (defined as $L = 2.5$ to 7) and (2) the L value at which the outer belt flux peaks (L_{max}). SAMPEX PET data overlap the ground-based chorus data from 2000 to 2004 and thus is only available for 100 out of the 144 storms analyzed.

3. Analysis

In order to examine the response of chorus waves as observed on the ground and the relationship with energetic electron populations during geomagnetic storms, we perform a set of superposed epoch analyses. For each, the $t = 0$ epoch is set to minimum Dst^* , and average values of the variables are computed at 30 min intervals. For the ground-based chorus measurements, values are only included in the superposed averaging if the station was in a local time sector where chorus is typically observed, which for

South Pole corresponds to the dayside hemisphere ($5 < \text{MLT} < 17$) and for Palmer the morning hemisphere ($0 < \text{MLT} < 12$) as seen in Figures 1b and 1c.

We examine four scenarios: (1) all storms versus random epochs (section 3.1), (2) large storms versus moderate storms (section 3.2), (3) CIR-driven storms versus CME-driven storms (section 3.3), and (4) storms classified as acceleration events versus nonevents (section 3.5). For each scenario, we perform statistical hypothesis testing, the Mann-Whitney U test [Mann and Whitney, 1947], to determine whether there is a statistically significant difference between the two populations that compose the superposed averages. A Mann-Whitney U test is performed every 12 h of epoch time, and $h = 1$ indicates that the null hypothesis (that the samples are drawn from distributions with equal medians) can be rejected at the 5% significance level.

3.1. All Storms

First, we examine the average response of geomagnetic indices, energetic electrons, and chorus waves over all 144 storms versus a set of 144 randomly selected epochs within the same overall time interval. In Figure 3, the average values for the random epochs are shown in black, and the storm averages are color coded with red, indicating intervals when the storm values are statistically significantly different from the random values ($h = 1$ for the Mann-Whitney U test), and blue indicating when there is no statistically significant difference between the two populations ($h = 0$). As one would expect, the values of Dst^* and Kp are larger during storm main phase and recovery than randomly selected intervals, and these differences are statistically significant (Figures 3a and 3b).

In terms of the energetic electrons, we see that both the >600 keV flux at geosynchronous (Figure 3c) and the 2–6 MeV flux averaged across the outer belt from SAMPEX (Figure 3d) become depleted during the main phase and reach a minimum value near minimum Dst^* . After several days of recovery, the fluxes at the geosynchronous orbit exceed those of the random intervals, but averaged across the outer belt, the fluxes recover with values that are statistically similar to the random intervals. Also, the L value, where the 2–6 MeV flux peaks (L_{max}), moves inward during storm main phase and early recovery (Figure 3e). As recovery proceeds, L_{max} moves outward again.

At the South Pole Station ($L > 9$), the occurrence of chorus dips strongly during storm main phase (Figure 3f), mimicking the general Kp dependence shown earlier. Smith *et al.* [2004a] in examining Halley Bay data ($L = 4.3$) also observed a dropout of power in the chorus band during the main phase, and the dropout was attributed to the disruption of ducted propagation paths to the ground by intense storm time electric fields. In contrast, at the higher- L South Pole Station, we attribute the dropout of chorus to a lack of chorus in the source region. As a result of strong driving conditions, the dayside magnetopause is eroded, and South Pole is likely situated well inside the polar cap and on open field lines during the main phase. During the storm recovery phase, there is no statistically significant difference in chorus occurrence (or amplitude, not shown) at the South Pole compared to random epochs.

On the other hand, both the occurrence and amplitude of chorus waves observed at the lower latitude Palmer Station ($L = 2.4$) are significantly enhanced over random epochs during storm main phase and for several days into recovery (Figures 3g and 3h). In contrast to Halley Bay, a main phase dropout is not seen in the Palmer data. (We note that the quantity most comparable to the analysis of Smith *et al.* [2004a] would be the product of occurrence and amplitude, which also does not exhibit a dropout.) On the other hand, we do observe that both chorus occurrence and amplitude are higher in the half day after minimum Dst^* than the half day before, despite stronger geomagnetic activity during the main phase.

We also note that the average duration of chorus activity increases at Palmer station during geomagnetic storms. The average duration of chorus activity, estimated by the average number of consecutive synoptic intervals with chorus events, is ~ 30 min at Palmer and ~ 2.75 h at the South Pole, but during storm intervals the average duration at Palmer is ~ 3 h while the duration at the South Pole is unchanged.

Due to the lack of enhancement of chorus observed at South Pole during storms, further analysis will focus solely on the lower L Palmer data. No statistically significant differences in chorus activity at South Pole were found in any of the subsequent analyses.

3.2. Large Storms Versus Moderate Storms

Next, we examine the effect of storm size on energetic electron populations and chorus activity at Palmer. We calculate the median value of minimum Dst^* (-77 nT) and divide the 144 storms into two equal cat-

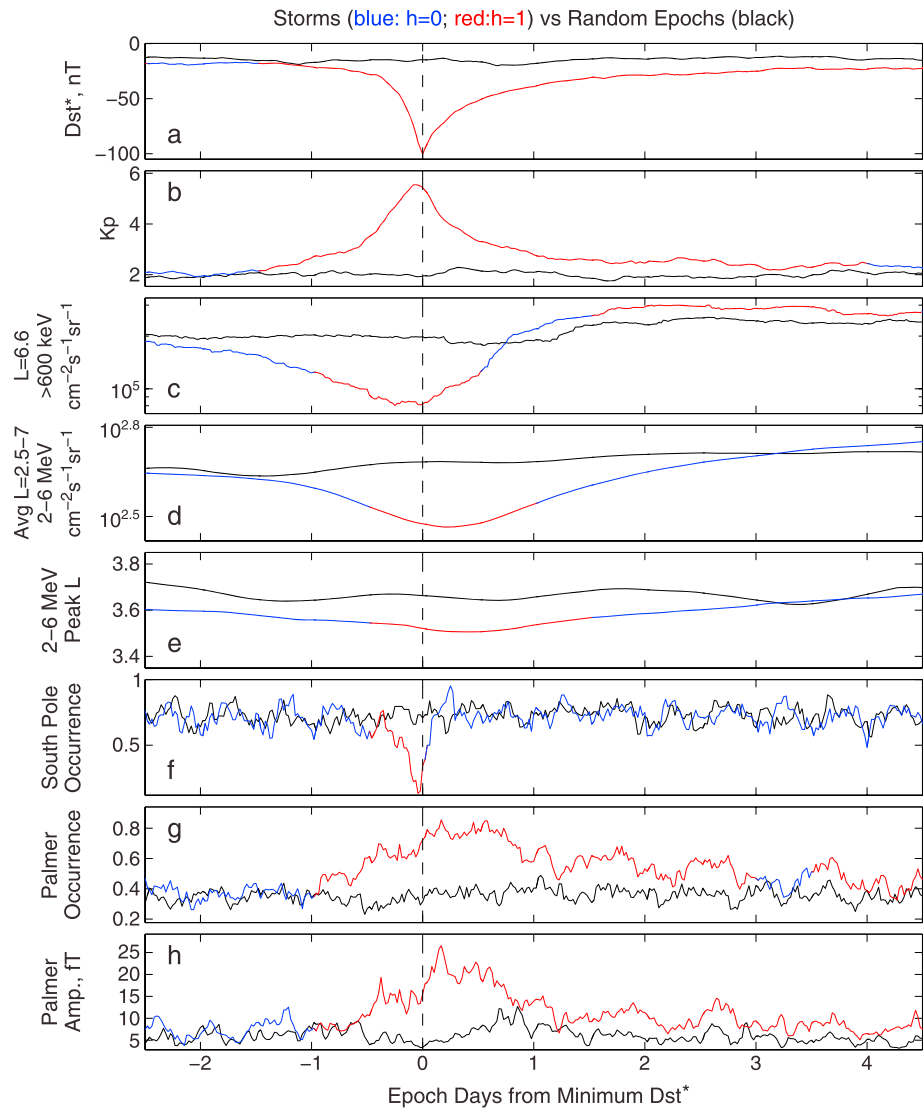


Figure 3. (a–h) Superposed epoch analysis comparing storm intervals (blue/red) to random epochs (black). The storm intervals are color-coded red for intervals when the values during storms are statistically significantly different than random intervals ($h = 1$ for the Mann-Whitney U test) and coded blue when storms are statistically indistinguishable from random intervals.

egories above (large storms) and below (moderate storms) the median. Figure 4 shows results of the superposed epoch analysis for large versus moderate storms.

In terms of the energetic electrons, we see that larger storms tend to result in deeper depletions in the electron flux both at geosynchronous orbit and averaged across the outer belt (Figures 4c and 4d). However, by 2 to 3 days after minimum Dst^* , there is no statistical difference between the flux resulting from large and moderate storms. This is consistent with past work showing that larger storms do not necessarily result to a more intense outer belt [Reeves *et al.*, 2003; Miyoshi and Kataoka, 2005; Zhao and Li, 2013]. However, the fact that larger storms have lower fluxes at the end of main phase suggests that there is more acceleration occurring during the recovery phase of the larger storms. The value of L_{max} is statistically significantly lower during the larger storms (Figure 4e), a trend that has also been reported in past work [Tverskaya *et al.*, 2003; Zhao and Li, 2013].

Chorus occurrence and amplitude at Palmer (Figures 4f and 4g) are significantly higher for large storms during both main and recovery phases. In Figure 4h, we have added the upper frequency cutoff of chorus at Palmer showing that chorus extends to higher frequency during more intense storms. As discussed

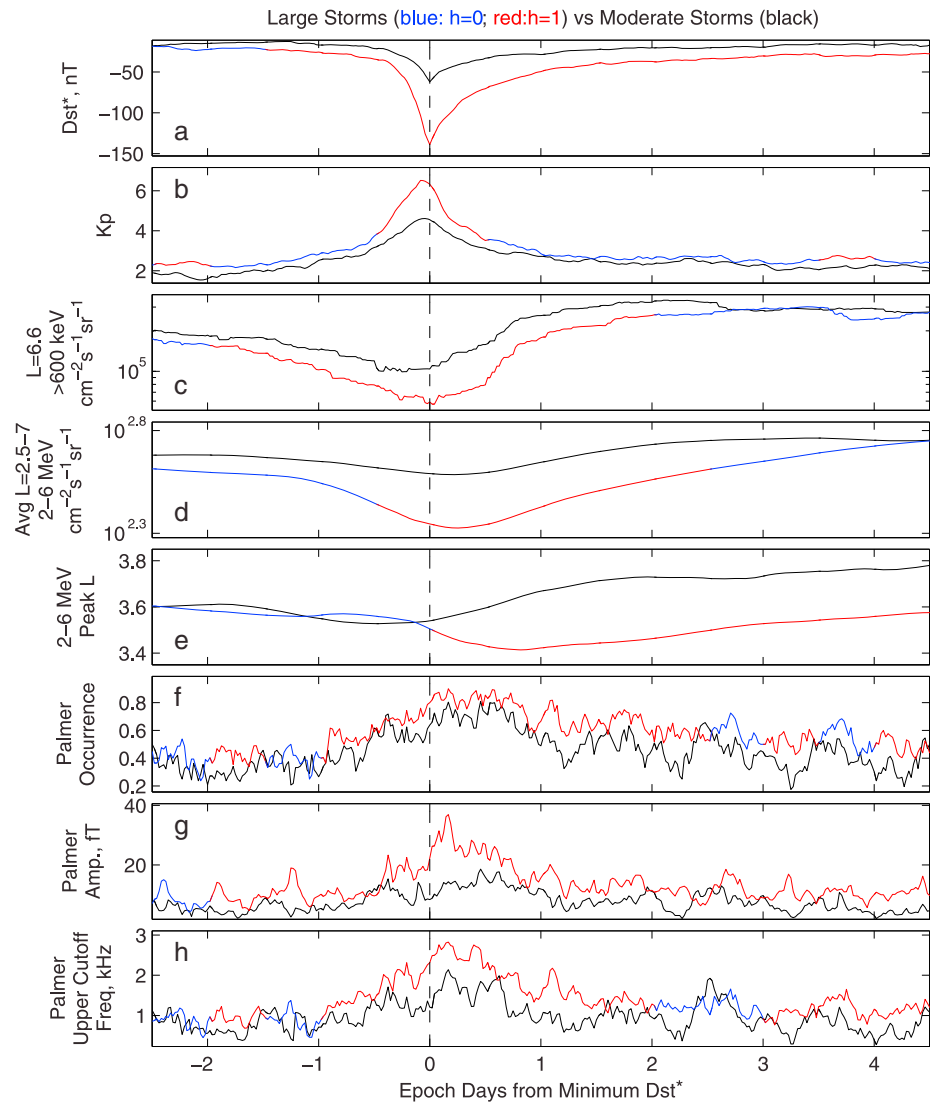


Figure 4. (a–h) Superposed epoch analysis comparing large storms with minimum $Dst^* > -77$ nT (blue/red) to moderate storms with minimum $Dst^* < -77$ nT (black).

in *Smith et al.* [2004a], the chorus frequency band scales with the equatorial electron gyrofrequency, and thus the observation of higher-frequency chorus suggests that the ground station is observing waves generated in the lower L portion of the station’s viewing area. *Smith et al.* [2004a] also observed an increase in chorus intensity in the higher-frequency channels during larger storms as observed at Halley Bay. However, *Smith et al.* [2004a] reported that in the 1 kHz band (where chorus at Halley is overall the most intense), there is no difference in intensity between large and moderate storms. This is in contrast to the results from Palmer where chorus is more intense during larger storms independent of the frequency band examined (not shown). Overall, we find that during large storms, chorus at Palmer occurs more frequently, has higher amplitude, and is generated at lower L shell than moderate storms, and these trends continue for several days into recovery.

3.3. CIR-Driven Versus CME-Driven Storms

Past work has shown that geomagnetic storm driven by CIR-associated solar wind structures are more likely to result in enhanced fluxes of energetic electrons at the end of the storm recovery phase [*Miyoshi and Kataoka*, 2005, 2011]. A confounding factor in differentiating storms by type is that CME storms are on average significantly larger [e.g., *Denton et al.*, 2006; *Turner et al.*, 2009]. To account for differences in storm size, we compare the set of all CIR storms to the set of CME storms where the minimum Dst^* is greater than

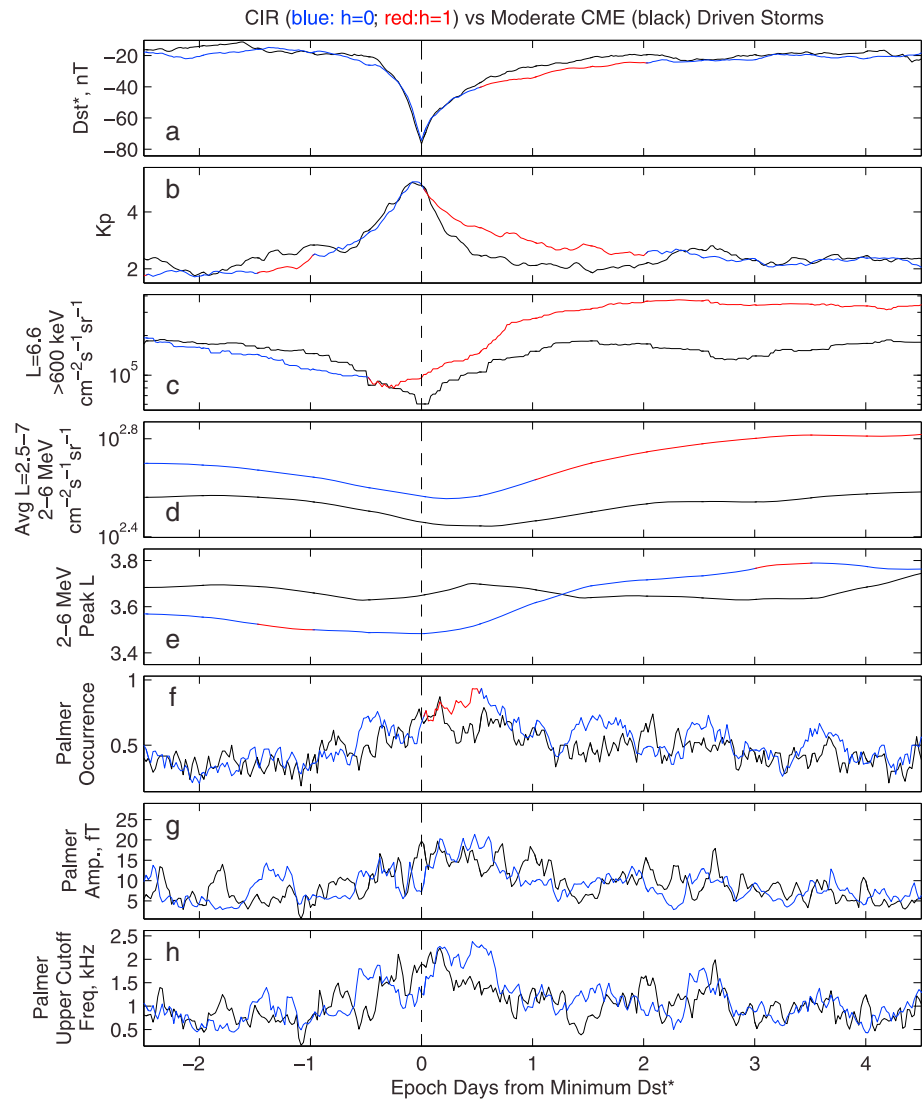


Figure 5. (a–h) Superposed epoch analysis comparing CIR-associated storms (blue/red) to CME-associated storms with minimum $Dst^* > -110$ nT (black).

–110 nT. Using this restriction, the two types of storms have similar average values of minimum Dst^* , but CIR storms tend to have more disturbed values of Dst^* and Kp during the recovery phase (Figures 5a and 5b), consistent with past work. In terms of energetic electrons, the CIR storms tend to have a higher flux in the recovery phase as seen at geosynchronous (Figure 5c) and averaged across the outer belt (Figure 5d). At Palmer, we see very little difference in chorus properties between the CIR and the moderate CME storms, with the exception of higher chorus occurrence in the half day after minimum Dst^* for the CIR events (Figure 5f).

3.4. Events Versus Nonevents

Next we perform an analysis similar to that of *Smith et al.* [2004b] and sort the storms strictly by the value of the geosynchronous electron flux several days into recovery. We divided the storms into two categories based on the median value of the > 600 keV flux 2.5 days after minimum Dst^* . Consistent with the convention of *Smith et al.* [2004b], storms with flux above the median value are dubbed events and those below the median are nonevents. Figure 6a shows that the average Dst^* signatures for events and nonevents are nearly identical, but the events tend to have elevated Kp for several days into recovery (Figure 6b). Per the definition of the categories, events have statistically significantly higher flux in the recovery phase both at geosynchronous orbit (Figure 6c) and averaged across the belt (Figure 6d), but we also note that events tend

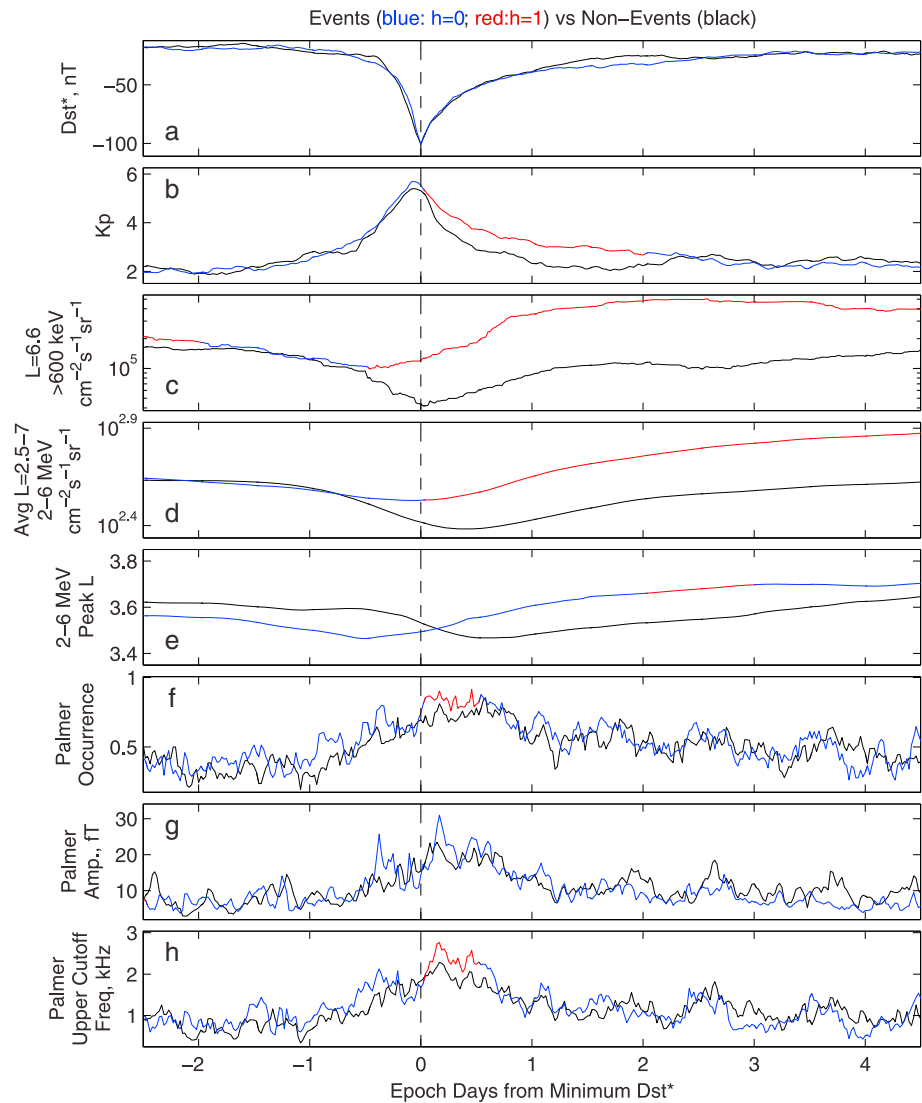


Figure 6. (a–h) Superposed epoch analysis comparing storms with higher geosynchronous flux 2.5 days after minimum Dst^* (events: blue/red) to those with lower flux (nonevents: black).

to have less loss during main phase and a higher flux value near minimum Dst^* . In terms of chorus observations at Palmer, we see that events have higher chorus occurrence (Figure 6f) and upper cutoff frequency (Figure 6h) in the half day after minimum Dst^* .

3.5. Acceleration Events Versus Nonevents

In the previous section, when sorting the storms by the value of the electron flux (events/nonevents) we found that storms that tend to have a higher flux 2.5 days into recovery also tend to have a higher flux at minimum Dst^* (Figures 6c and 6d). Thus, it is unclear whether the processes that drive electron acceleration are more active during events or whether there is simply less loss during main phase as compared with nonevents and a similar amount of acceleration during recovery. This can also be seen in the breakdown by CIR/CME storms where at geosynchronous orbit, the CIR storms have higher poststorm fluxes but also higher flux at minimum Dst^* (Figure 5c). Conversely, large and moderate storms result in, on average, nearly equal fluxes after recovery, but large storms experience more losses during main phase (Figures 4c and 4d), suggesting that acceleration processes are more active during the recovery phase of large storms. We construct a metric to attempt to select storms where the acceleration processes in the recovery phase appear to be most active. We do this by examining the slope of the flux during recovery and divide the storms into acceleration and nonacceleration events.

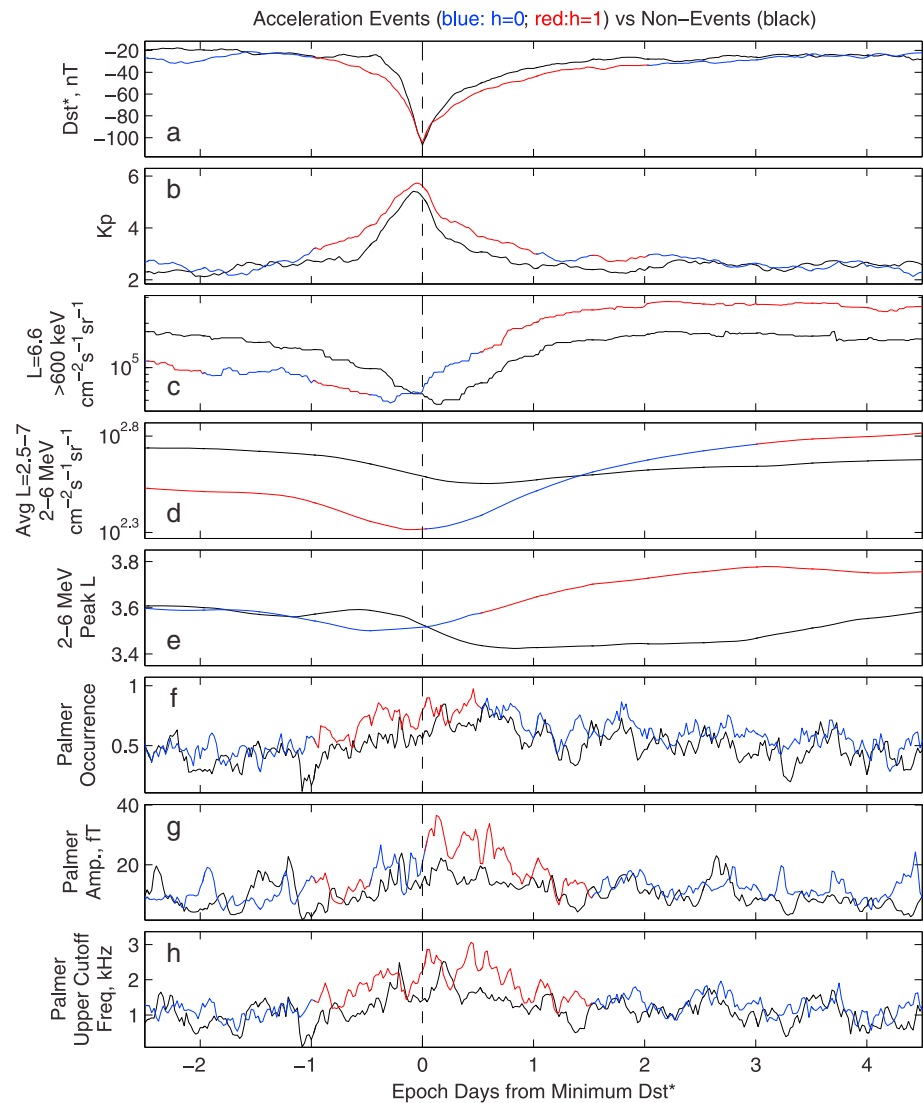


Figure 7. (a–h) Superposed epoch analysis comparing storms with a higher ratio of flux averaged across the outer belt at recovery to flux at minimum Dst^* (acceleration events: blue/red) to those with a lower ratio (nonevents: black).

For each of the 100 storms observed by SAMPEX, we compute the ratio of the 2–6 MeV electron flux averaged across the outer belt at the end of the recovery phase (defined previously as when Dst^* recovers 80% from the minimum value) to the value at minimum Dst^* . The median value for this ratio is 1.5, and we divide the storms into two equal categories above (acceleration events) and below (nonevents) the median. By using the flux at the end of the recovery phase, this metric takes into account the variable length of geomagnetic storms, which for this set of storms varies from 0.4 to 10 days (median: 1.9, mean: 2.6 days). In the superposed epoch analysis of acceleration events and nonevents, we find that average values of Dst^* and Kp tend to be more disturbed for acceleration events during both main phase and recovery (Figures 7a and 7b), but the average values of minimum Dst^* are similar. At geosynchronous orbit, the electron flux at minimum Dst^* is similar between the two categories, but during recovery phase, the flux rises to statistically significantly higher values for the acceleration events (Figure 7c). Averaged across the belt, the nonacceleration events tend to be the events for which there is very little loss of electrons in the interval surrounding minimum Dst^* and subsequently relatively little increase in the flux during recovery (Figure 7d). On the other hand, the acceleration events tend to have large flux decreases during main phase and a steady rise during recovery. The value of L_{max} is similar for the two types of storms during main phase and early recovery but moves to higher L for the acceleration events later in recovery (Figure 7e).

At Palmer, for storms categorized as acceleration events, we observe statistically significant increases in the occurrence, amplitude, and upper cutoff frequency of chorus waves during main phase and early recovery (Figures 7f–7h). After about 1.5 days after minimum Dst^* , the properties of chorus are similar between acceleration events and nonevents.

3.6. Influence of Day-Night Ionospheric Conditions

As mentioned previously, ground-based wave observations are challenging to interpret and to directly related to wave activity in the magnetosphere due to several distinct effects of wave propagation. Chorus observed at Palmer Station is believed to have a source region near the geomagnetic equator [e.g., *LeDocq et al.*, 1998; *Santolik et al.*, 2004], whereas the source region for waves observed at South Pole may extend to higher latitudes [e.g., *Tsurutani and Smith*, 1977; *Spasojevic and Inan*, 2010; *Katoh and Omura*, 2013]. Once generated, the waves can propagate in either a ducted [*Helliwell*, 1965, section 3.6] or nonducted [*Chum and Santolik*, 2005; *Golden et al.*, 2010] mode toward the topside ionosphere. In the off-equatorial region, Landau damping due to the suprathermal electron distribution becomes important particularly for the nonducted waves, and the amount of damping is expected to be geomagnetically dependent [*Li et al.*, 2010a]. Detailed examination of nonducted propagation, including the effects of Landau damping, as it relates to ground observations of chorus at Palmer station was performed by *Golden et al.* [2010]. Waves that reach the topside ionosphere with wave normal angles within the relatively narrow ionospheric transmission cone [*Helliwell*, 1965, section 3.7] or that are scattered into the transmission cone by F region density irregularities [*Walker*, 1974; *Sonwalkar and Harikumar*, 2000] can propagate through the ionosphere but undergo transionospheric attenuation that is dependent on latitude, season, time of day, and geomagnetic conditions [*Graf et al.*, 2013]. Finally, waves that exit the ionosphere some distance from the station propagate in the Earth-ionosphere waveguide with attenuation up to 7 dB per 100 km close to the ionospheric exit point and a few dB per 1000 km at further distances [*Walker*, 1974; *Tsuruda et al.*, 1982]. For a given ground-based wave measurement, the propagation path from the source region to the station is unknown, and few studies have directly compared in situ and ground-based observations. Notably, *Golden et al.* [2012a] performed a statistical analysis of hiss as observed on the ground at Palmer and in situ by the Time History of Events and Macroscale Interactions during Substorms spacecraft. They evaluated the utility of ground-based measurements in predicting in situ amplitudes and found that the results depended strongly on both local time and day-night ionospheric conditions.

In the analysis presented in the previous sections, we treated all wave observations equally and did not attempt to account for differences in the propagation path. In this section, we explore differences due to day-night conditions at Palmer (which affects both transionospheric and subionospheric propagation) and its influence on the observed amplitude. *Graf et al.* [2013] used the full wave model of *Lehtinen and Inan* [2008, 2009] to provide estimates of transionospheric attenuation to update the curves of *Helliwell* [1965, section 3.7]. At the geomagnetic latitude of Palmer and for a wave frequency of 2 kHz, *Graf et al.* [2013] estimated that the total ionospheric attenuation is ~ 3 –8 dB higher under day conditions than under night conditions. For the Palmer Station chorus database, the normalized occurrence of chorus under day versus night conditions is essentially identical, 6.26% occurrence for day (defined as sunlight at 100 km altitude) and 6.29% for night. However, the average amplitude across all day measurements is 1.9 dB lower than the average across all night measurements. We note that at South Pole, the observed average day-night difference of 0.56 dB is also lower than the *Graf et al.* [2013] prediction of ~ 2 –6 dB. Figure 8 shows the distributions of chorus amplitude under (a) day and (b) night conditions. Figure 8c shows how the difference in the average amplitude changes over the year with a maximum in day-night difference in the Southern Hemisphere winter months and minimum in Southern Hemisphere summer months. There are few night hours (due to the restriction of no sunlight at 100 km) and no night chorus events from day of year 0 to 60 and 300 to 365. We also examined the difference in day-night amplitude as a function of Kp but found no clear trend.

In order to account for day-night differences in our analysis of geomagnetic storms, we scaled the Palmer night measurements by the average day-night difference as a function of day of year derived in Figure 8c. For days 60 to 90 the average difference was found to be +0.2 dB (day events were on average stronger), but we used instead a value of 0 dB since the observational result does not meet general expectations and may have been skewed by the small number of night events in this bin. After scaling the night amplitudes, we recomputed the superposed averages and the statistical hypothesis tests, and we present comparisons for our key results in Figures 8d–8f. The solid-colored line in Figure 8d is identical to the colored line in

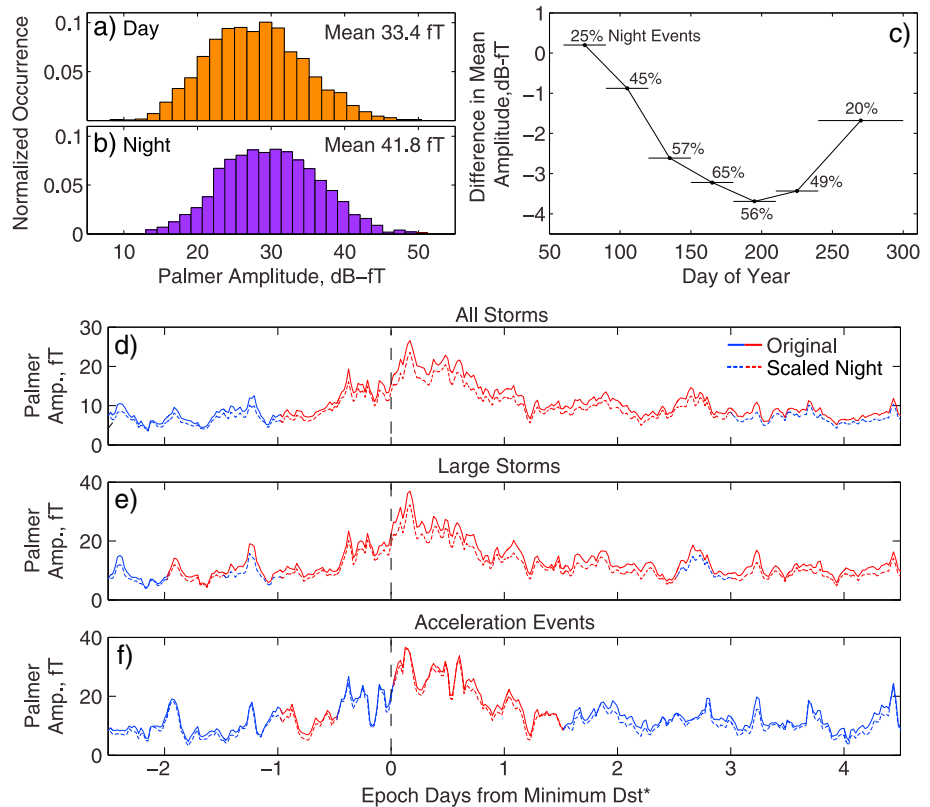


Figure 8. Distribution of chorus amplitude observed during (a) day and (b) night ionospheric conditions at Palmer Station. (c) Difference in the average day-night amplitude as a function of day of year. The horizontal lines indicate the days over which the average is taken, and the percentage of night observations for each day range is indicated. Superposed epoch analysis comparing the original amplitudes (solid) with the averages including scaling of the night measurement (dashed) for (d) all storms, (e) large storms, and (f) acceleration events. The results of the statistical hypothesis test comparing the distributions contained in the averages between random epochs (Figure 8d), moderate storms (Figure 8e), and non-events (Figure 8f) are color coded (blue: $h = 0$; red: $h = 1$).

Figure 3h (superposed epoch of storms versus random epochs). The dashed line is the average for all storms performed after scaling downward the night measurements. For clarity, the superposed averages for the random epochs are not shown (black curve in Figure 3h and corresponding dashed curved for averages after scaling), but the result of the statistical hypothesis test are color coded. Scaling the night events results is a slightly lower average amplitude, but during storm main phase and for 3 days into recovery, the storm amplitudes are still statistically significantly higher than random epochs. After scaling, however, from day 3 onward, the storm intervals are statistically no different than random intervals (dashed curve changes from red to blue).

Figure 8e performs the same comparison as Figure 4g (large storms versus moderate storms). Here we find that the night event scaling affects brief intervals of statistical significance (blue dashed curve for days -1.5 to -1 and days 2 to 2.5), but the overall result of higher amplitudes during the main and recovery phases of larger storms holds. Figure 8f shows the comparison for Figure 7g (acceleration events versus nonevents), and here there are no changes to the statistical significance after scaling the night measurements.

In summary, the normalized occurrence of chorus events at Palmer is not affected by day-night ionospheric conditions, but the event amplitude is on average ~ 2 dB higher during night conditions and exhibits seasonal dependence. If we scale downward the amplitude of the night events by a seasonally dependent factor, we find that the results of the statistical hypothesis testing are essentially identical with the exception that when comparing storms versus random epochs, there is a statistically significantly higher amplitude for only 3 days into recovery rather than >4 days seen before the amplitude scaling was applied.

4. Discussion

Long data records from ground-based ELF/VLF receivers are used to statistically examine the response of magnetospheric chorus emissions to different types of geomagnetic storms and the relationship to changes in the outer belt electron population. Chorus waves have a high occurrence in the outer dayside magnetosphere with South Pole Station ($L > 9$) observing chorus on ~80% of days when traversing the noon sector. However, during the main phase of geomagnetic storms, there is a significant dropout in the wave occurrence at South Pole (Figure 3f), which is attributed to compression and erosion of the dayside magnetosphere that places South Pole either on open magnetic field lines poleward of the chorus source region or on field lines that extend to large ($> 15 R_E$) distances in the flanks of the magnetotail (Figure 2). Specifically, when the station is in the noon sector, we find a strong negative correlation between the equatorward distance to the nearest closed field and the occurrence of chorus at South Pole (Figures 2b and 2c). During storm recovery phase, there is no statistically significant difference between chorus occurrence and amplitude at South Pole as compared to random epoch intervals (Figure 3f). The magnetospheric chorus population observed at South Pole is not driven by storm-time activity, and chorus in the outer dayside magnetosphere likely does not play a role in the recovery of outer belt.

At the lower latitude Palmer Station ($L = 2.4$), the occurrence and amplitude of chorus waves are significantly enhanced during the main and recovery phases of geomagnetic storms (Figures 3g and 3h). In contrast to the observations at South Pole and Halley Bay ($L = 4.3$), there is no dropout in wave activity during main phase. *Smith et al.* [2004a] discussed several possibilities but primarily attributed the main phase chorus dropout at Halley to the disruption of ducted paths to ground by strong storm time electric fields. In Figure 2a, we explored another possibility, that is, how the changing geomagnetic field configuration with increasing activity influences the ELF/VLF viewing area of the stations. At Halley Bay, the field lines passing through the ground station on the nightside become dramatically stretched under disturbed geomagnetic conditions and map to distances $> 10 R_E$, well outside the chorus source region. Measurements at geosynchronous orbit are similarly influenced by the stretched magnetic field configuration since it does not generally lie in the magnetic equatorial plane, and *MacDonald et al.* [2008] reported that the conditions for whistler-mode growth at geosynchronous orbit near midnight during main phase are also reduced. In contrast, the magnetic mapping of Palmer is not strongly influenced by geomagnetic activity level, and the main phase chorus observed at Palmer is likely representative of activity in the inner magnetospheric source region.

Chorus activity at Palmer exhibits a maximum in occurrence, amplitude, and upper cutoff frequency in the early recovery phase of geomagnetic storms (within a half a day of minimum Dst^*) despite the fact that, on average, the Kp and Dst^* indices are more disturbed during main phase (Figures 3g and 3h). It is difficult to assess whether the slightly weaker chorus activity during main phase (relative to amount of geomagnetic activity) reflects conditions in the source region or is the result of another effect such as a disruption in propagation to ground. Statistical studies of chorus activity [*Meredith et al.*, 2001; *Li et al.*, 2009; *Bunch et al.*, 2012; *Agapitov et al.*, 2013] primarily bin the data by the instantaneous (or average within several hours) value of an index (typically AE), and this will act to average out any subtle storm-phase-dependent effects. *Golden et al.* [2012b] constructed a dynamic chorus model from spacecraft data driven by the time history of solar wind and geomagnetic conditions, but the input data were from 2008 to 2011, an interval with insufficient storm-time statistics. Therefore, further work is needed to understand if the observed strengthening in chorus activity during early recovery phase as observed at Palmer reflects enhanced conditions for growth in the magnetosphere.

In comparing large storms ($Dst^* < -77$ nT) to moderate storms ($Dst^* > -77$ nT), we find that the occurrence, amplitude, and upper cutoff frequency of chorus at Palmer are all significantly enhanced during large storms (Figures 4f–4h). The increase in the upper cutoff frequency is attributed to the inward motion of the plasmapause and the generation of waves at lower L values and was also reported in *Smith et al.* [2004a]. However, in the lower frequency band (1 kHz) where chorus is most intense overall, *Smith et al.* [2004a] reported that the wave intensity was independent of storm size. The difference in chorus intensity as a function of storm size between the two stations is somewhat puzzling, but it is possible that the deep inward motion of the plasmasphere during large storms results in more chorus activity within the ELF/VLF viewing area of the

station. On the other hand, the ELF/VLF viewing area of Halley Bay at higher L is less influenced by the location of the plasmopause.

Smith et al. [2004b] examined storms with and without enhancements in the geosynchronous 1.8–3.5 MeV electron flux (events and nonevents) and reported that the response of chorus at Halley Bay is frequency dependent. In the lower frequency bands (0.5–1 kHz), recovery phase chorus power is higher during storms that result to higher poststorm electron fluxes, and the authors cite this as evidence of chorus-driven electron acceleration. On the other hand, at higher frequencies (near 2 kHz), the non-events are associated with higher chorus intensity particularly in the early recovery phase, but this association is disregarded as a propagation effect resulting from the cutoff of the higher-frequency wave source region by rapidly recovering plasmopause. However, it is unclear why this propagation effect would only be attributed to non-events particularly since the authors report that there is no correlation between storm intensity and electron flux enhancements.

We performed a similar analysis to that of *Smith et al.* [2004b] and separated the storms by the absolute flux level after several days of recovery. We found that, on average, storms with higher recovery phase fluxes tended to be storms with lower amounts of loss during main phase (Figures 6c and 6d), similar to the trend at geosynchronous orbit in the comparison of CIR and CME storms in Figure 5c. We concluded that storms with the highest recovery phase flux do not necessarily represent storms where acceleration processes are most active, and we instead developed a new metric to partitioned storms based on the slope of the flux in the recovery phase.

During the recovery phase of storms that we categorize as acceleration events, the occurrence, amplitude and upper cutoff frequency of chorus as measured at Palmer are statistically significantly enhanced for about a day and a half after minimum Dst^* . Our analysis suggests that during acceleration events, chorus may be more intense in the source region and that the source region extends to lower L . Both of these factors result in favorable conditions for chorus-driven electron acceleration, and the duration of the chorus enhancements observed at Palmer are consistent with theoretical calculations of the required diffusion timescales [*Horne et al.*, 2005; *Shprits et al.*, 2009].

5. Conclusions

We performed superposed epoch analysis and statistical hypothesis testing to examine the properties of chorus as observed by ground-based receivers as a function of storm phase, storm size, and storm type, and the rate of energetic electron flux increase during recovery.

1. During the main phase of geomagnetic storms, there is a dropout of chorus activity as observed on the ground at South Pole Station ($L > 9$) and is attributed to the region being either on open field lines or on field lines that map to large distances in the flanks of the magnetotail.
2. During the recovery phase of geomagnetic storms, there is no enhancement in chorus activity compared with random intervals as observed on the ground at South Pole.
3. At Palmer Station (located at $L = 2.4$, but with an ELF/VLF area extending to $L \approx 5$), chorus is strongly enhanced during both the main and recovery phases of storms. The occurrence, amplitude, and upper cutoff frequency of chorus all peak in early recovery phase, within less than half a day of minimum Dst^* .
4. During storm main phase, chorus at Palmer occurs more frequently, is more intense, and extends to higher frequency during larger geomagnetic storms. Larger storms also tend to result in larger depletions of electrons by the end of main phase as observed at geosynchronous and averaged across the outer belt.
5. During storm recovery phase, chorus at Palmer occurs more frequently, is more intense, and extends to higher frequency during larger geomagnetic storms, and storms where the rate of electron flux increase, averaged across the outer belt, is the higher.
6. CIR storms tend to result in a higher flux of electrons in the outer belt, but we find little difference in chorus activity at Palmer between CIR storms and CME storms of equal average strength.
7. When separating storms by the absolute flux level during recovery, we find that storms with the higher recovery phase flux tend to also have higher flux near minimum Dst^* . For events with higher recovery phase flux, chorus occurrence and upper cutoff frequency at Palmer are briefly enhanced during early recovery phase.

Acknowledgments

This work was supported by the National Science Foundation under awards 1043442 and 1141791 to Stanford University. We thank Ian Richardson for providing the list of solar wind structures. The geomagnetic indices were provided by the Kyoto World Data Center. The solar wind data were derived from data on OMNIWeb, provided by Richard Denton and Zhengui Qin, and accessed through the Virtual Radiation Belt Observatory. The GOES spacecraft data were provided by the NOAA Space Weather Prediction Center. All data used in this study can be accessed through the sources listed above or by contacting the author.

Michael Liemohn thanks Reinhard Friedel and two other reviewers for their assistance in evaluating this paper.

References

- Agapitov, O., A. Artemyev, V. Krasnoselskikh, Y. V. Khotyaintsev, D. Mourenas, H. Breuillard, M. Balikhin, and G. Rolland (2013), Statistics of whistler mode waves in the outer radiation belt: Cluster STAFF-SA measurements, *J. Geophys. Res. Space Physics*, *118*, 3407–3420, doi:10.1002/jgra.50312.
- Albert, J. M., N. P. Meredith, and R. B. Horne (2009), Three-dimensional diffusion simulation of outer radiation belt electrons during the 9 October 1990 magnetic storm, *J. Geophys. Res.*, *114*, A09214, doi:10.1029/2009JA014336.
- Baker, D. N., G. M. Mason, O. Figueroa, G. Colon, J. G. Watzin, and R. M. Aleman (1993), An overview of the Solar, Anomalous, and Magnetospheric Particle Explorer (SAMPEX) mission, *IEEE Trans. Geosci. Remote Sens.*, *31*, 531–541, doi:10.1109/36.225519.
- Bunch, N. L., M. Spasojevic, and Y. Y. Shprits (2011), On the latitudinal extent of chorus emissions as observed by the polar plasma wave instrument, *J. Geophys. Res.*, *116*, A04204, doi:10.1029/2010JA016181.
- Bunch, N. L., M. Spasojevic, and Y. Y. Shprits (2012), Off-equatorial chorus occurrence and wave amplitude distributions as observed by the polar plasma wave instrument, *J. Geophys. Res.*, *117*, A04205, doi:10.1029/2011JA017228.
- Chum, J., and O. Santolik (2005), Propagation of whistler-mode chorus to low altitudes: Divergent ray trajectories and ground accessibility, *Ann. Geophys.*, *23*, 3727–3738.
- Cohen, M. B., U. S. Inan, and E. W. Paschal (2010), Sensitive broadband ELF/VLF radio reception with the awesome instrument, *IEEE Trans. Geosci. Remote Sens.*, *48*, 3–17, doi:10.1109/TGRS.2009.2028334.
- Denton, M. H., J. E. Borovsky, R. M. Skoug, M. F. Thomsen, B. Lavraud, M. G. Henderson, R. L. McPherron, J. C. Zhang, and M. W. Liemohn (2006), Geomagnetic storms driven by ICME- and CIR-dominated solar wind, *J. Geophys. Res.*, *111*, A07S07, doi:10.1029/2005JA011436.
- Golden, D., M. Spasojevic, F. R. Foust, N. G. Lehtinen, N. P. Meredith, and U. S. Inan (2010), Role of the plasmaphase in dictating the ground accessibility of ELF/VLF chorus, *J. Geophys. Res.*, *115*, A11211, doi:10.1029/2010JA015955.
- Golden, D., M. Spasojevic, and U. S. Inan (2011), Determination of solar cycle variations of midlatitude ELF/VLF chorus and hiss via automated signal detection, *J. Geophys. Res.*, *116*, A03225, doi:10.1029/2010JA016193.
- Golden, D. I., M. Spasojevic, W. Li, and Y. Nishimura (2012a), Statistical modeling of in situ hiss amplitudes using ground measurements, *J. Geophys. Res.*, *117*, A05218, doi:10.1029/2011JA017376.
- Golden, D. I., M. Spasojevic, W. Li, and Y. Nishimura (2012b), An empirical model of magnetospheric chorus amplitude using solar wind and geomagnetic indices, *J. Geophys. Res.*, *117*, A12204, doi:10.1029/2012JA018210.
- Graf, K. L., N. G. Lehtinen, M. Spasojevic, M. B. Cohen, R. A. Marshall, and U. S. Inan (2013), Analysis of experimentally validated trans-ionospheric attenuation estimates of VLF signals, *J. Geophys. Res. Space Physics*, *118*, 2708–2720, doi:10.1002/jgra.50228.
- Harriman, S. K. (2010), Custom integrated amplifier chip for VLF magnetic receiver, PhD thesis, Department of Electrical Engineering, Stanford Univ., Stanford, Calif.
- Helliwell, R. A. (1965), *Whistlers and Related Ionospheric Phenomena*, Stanford Univ. Press, Stanford, Calif.
- Horne, R. B., R. M. Thorne, S. A. Glauert, J. M. Albert, N. P. Meredith, and R. R. Anderson (2005), Timescale for radiation belt electron acceleration by whistler mode chorus waves, *J. Geophys. Res.*, *110*, A03225, doi:10.1029/2004JA010811.
- Katoh, Y., and Y. Omura (2013), Effect of the background magnetic field inhomogeneity on generation processes of whistler-mode chorus and broadband hiss-like emissions, *J. Geophys. Res. Space Physics*, *118*, 4189–4198, doi:10.1002/jgra.50395.
- Keika, K., M. Spasojevic, W. Li, J. Bortnik, Y. Miyoshi, and V. Angelopoulos (2012), Penguin/ago and THEMIS conjugate observations of whistler mode chorus waves in the dayside uniform zone under steady solar wind and quiet geomagnetic conditions, *J. Geophys. Res.*, *117*, A07212, doi:10.1029/2012JA017708.
- LeDocq, M. J., D. A. Gurnett, and G. B. Hospodarsky (1998), Chorus source locations from VLF poynting flux measurements with the polar spacecraft, *Geophys. Res. Lett.*, *25*, 4063–4066, doi:10.1029/1998GL900071.
- Lehtinen, N. G., and U. S. Inan (2008), Radiation of ELF/VLF waves by harmonically varying currents into a stratified ionosphere with application to radiation by a modulated electrojet, *J. Geophys. Res.*, *113*, A06301, doi:10.1029/2007JA012911.
- Lehtinen, N. G., and U. S. Inan (2009), Full-wave modeling of transionospheric propagation of VLF waves, *Geophys. Res. Lett.*, *36*, L03104, doi:10.1029/2008GL036535.
- Li, W., Y. Y. Shprits, and R. M. Thorne (2007), Dynamic evolution of energetic outer zone electrons due to wave-particle interactions during storms, *J. Geophys. Res.*, *112*, A10220, doi:10.1029/2007JA012368.
- Li, W., R. M. Thorne, V. Angelopoulos, J. Bortnik, C. M. Cully, B. Ni, O. LeContel, A. Roux, U. Auster, and W. Magnes (2009), Global distribution of whistler-mode chorus waves observed on the THEMIS spacecraft, *Geophys. Res. Lett.*, *36*(9), L09104, doi:10.1029/2009GL037595.
- Li, W., R. M. Thorne, J. Bortnik, Y. Nishimura, V. Angelopoulos, L. Chen, J. P. McFadden, and J. W. Bonnell (2010a), Global distributions of suprathermal electrons observed on THEMIS and potential mechanisms for access into the plasmasphere, *J. Geophys. Res.*, *115*, A00J10, doi:10.1029/2010JA015687.
- Li, W., et al. (2010b), THEMIS analysis of observed equatorial electron distributions responsible for the chorus excitation, *J. Geophys. Res.*, *115*, A00F11, doi:10.1029/2009JA014845.
- Lorentzen, K. R., J. B. Blake, U. S. Inan, and J. Bortnik (2001), Observations of relativistic electron microbursts in association with VLF chorus, *J. Geophys. Res.*, *106*, 6017–6027, doi:10.1029/2000JA003018.
- MacDonald, E. A., M. H. Denton, M. F. Thomsen, and S. P. Gary (2008), Superposed epoch analysis of a whistler instability criterion at geosynchronous orbit during geomagnetic storms, *J. Atmos. Sol. Terr. Phys.*, *70*, 1789–1796, doi:10.1016/j.jastp.2008.03.021.
- Mann, H. B., and D. R. Whitney (1947), On a test of whether one of two random variables is stochastically larger than the other, *Ann. Math. Stat.*, *18*, 50–60.
- Mauk, B. H., N. J. Fox, S. G. Kanekal, R. L. Kessel, D. G. Sibeck, and A. Ukhorskiy (2012), Science objectives and rationale for the radiation belt storm probes mission, *Space Sci. Rev.*, *179*, 3–27, doi:10.1007/s11214-012-9908-y.
- McCullough, J. P., S. R. Elkington, and D. N. Baker (2012), The role of Shabansky orbits in compression-related electromagnetic ion cyclotron wave growth, *J. Geophys. Res.*, *117*, A01208, doi:10.1029/2011JA016948.
- Meredith, N. P., R. B. Horne, and R. R. Anderson (2001), Substorm dependence of chorus amplitudes: Implications for the acceleration of electrons to relativistic energies, *J. Geophys. Res.*, *106*, 13,165–13,178, doi:10.1029/2000JA900156.
- Millan, R. M., and D. N. Baker (2012), Acceleration of particles to high energies in Earth's radiation belts, *Space Sci. Rev.*, *173*, 103–131, doi:10.1007/s11214-012-9941-x.
- Millan, R. M., and R. M. Thorne (2007), Review of radiation belt relativistic electron losses, *J. Atmos. Sol. Terr. Phys.*, *69*, 362–377, doi:10.1016/j.jastp.2006.06.019.
- Min, K., J. Lee, and K. Keika (2010), Chorus wave generation near the dawnside magnetopause due to drift shell splitting of substorm-injected electrons, *J. Geophys. Res.*, *115*, A00I02, doi:10.1029/2010JA015474.
- Miyoshi, Y., and R. Kataoka (2005), Ring current ions and radiation belt electrons during geomagnetic storms driven by coronal mass ejections and corotating interaction regions, *Geophys. Res. Lett.*, *32*, L21105, doi:10.1029/2005GL024590.

- Miyoshi, Y., and R. Kataoka (2011), Solar cycle variations of outer radiation belt and its relationship to solar wind structure dependences, *J. Atmos. Sol. Terr. Phys.*, *73*, 77–87, doi:10.1016/j.jastp.2010.09.031.
- Ni, B., R. M. Thorne, N. P. Meredith, R. B. Horne, and Y. Y. Shprits (2011), Resonant scattering of plasma sheet electrons leading to diffuse auroral precipitation: 2. Evaluation for whistler mode chorus waves, *J. Geophys. Res.*, *116*, A04219, doi:10.1029/2010JA016233.
- O'Brien, T. P., and R. L. McPherron (2000), An empirical phase space analysis of ring current dynamics: Solar wind control of injection and decay, *J. Geophys. Res.*, *105*, 7707–7719, doi:10.1029/1998JA000437.
- Onsager, T., R. Grubb, J. Kunches, L. Matheson, D. Speich, R. W. Zwickl, and H. Sauer (1996), Operational uses of the GOES energetic particle detectors, in *GOES-8 and Beyond*, vol. 2812, edited by E. R. Washwell, pp. 281–290, SPIE Conf. Proc., Bellingham, Wash., doi:10.1117/12.254075.
- Orlova, K. G., and Y. Y. Shprits (2010), Dependence of pitch-angle scattering rates and loss timescales on the magnetic field model, *Geophys. Res. Lett.*, *37*, L05105, doi:10.1029/2009GL041639.
- Orlova, K. G., Y. Y. Shprits, and B. Ni (2012), Bounce-averaged diffusion coefficients due to resonant interaction of the outer radiation belt electrons with oblique chorus waves computed in a realistic magnetic field model, *J. Geophys. Res.*, *117*, A07209, doi:10.1029/2012JA017591.
- Petrinec, S. M., and C. T. Russell (1993), External and internal influences on the size of the dayside terrestrial magnetosphere, *Geophys. Res. Lett.*, *20*, 339–342, doi:10.1029/93GL00085.
- Pope, J. (1960), Effect of latitude on the diurnal maximum of "dawn chorus," *Nature*, *185*, 87–88.
- Qin, Z., R. E. Denton, N. A. Tsyganenko, and S. Wolf (2007), Solar wind parameters for magnetospheric magnetic field modeling, *Space Weather*, *5*, S11003, doi:10.1029/2006SW000296.
- Reeves, G., K. L. McAdams, R. H. W. Friedel, and T. P. O'Brien (2003), Acceleration and loss of relativistic electrons during geomagnetic storms, *Geophys. Res. Lett.*, *30*(10), 1529, doi:10.1029/2002GL016513.
- Richardson, I., H. Cane, and E. Cliver (2002), Sources of geomagnetic activity during nearly three solar cycles (1972–2000), *J. Geophys. Res.*, *107*(A8), 1187, doi:10.1029/2001JA000504.
- Richardson, I. G., E. W. Cliver, and H. V. Cane (2000), Sources of geomagnetic activity over the solar cycle: Relative importance of coronal mass ejections, high-speed streams, and slow solar wind, *J. Geophys. Res.*, *105*, 18,203–18,213, doi:10.1029/1999JA000400.
- Santolik, O., D. A. Gurnett, and J. Pickett (2004), Multipoint investigation of the source region of storm-time chorus, *Ann. Geophys.*, *22*, 2555–2563, doi:10.5194/angeo-22-2555-2004.
- Shprits, Y. Y., R. M. Thorne, R. B. Horne, and D. Summers (2006), Bounce-averaged diffusion coefficients for field-aligned chorus waves, *J. Geophys. Res.*, *111*, A10225, doi:10.1029/2006JA011725.
- Shprits, Y. Y., N. P. Meredith, and R. M. Thorne (2007), Parameterization of radiation belt electron loss timescales due to interactions with chorus waves, *Geophys. Res. Lett.*, *34*, L11110, doi:10.1029/2006GL029050.
- Shprits, Y. Y., S. R. Elkington, N. P. Meredith, and D. A. Subbotin (2008a), Review of modeling of losses and sources of relativistic electrons in the outer radiation belt I: Radial transport, *J. Atmos. Sol. Terr. Phys.*, *70*, 1679–1693, doi:10.1016/j.jastp.2008.06.008.
- Shprits, Y. Y., D. A. Subbotin, N. P. Meredith, and S. R. Elkington (2008b), Review of modeling of losses and sources of relativistic electrons in the outer radiation belt II: Local acceleration and loss, *J. Atmos. Sol. Terr. Phys.*, *70*, 1694–1713, doi:10.1016/j.jastp.2008.06.014.
- Shprits, Y. Y., D. Subbotin, and B. Ni (2009), Evolution of electron fluxes in the outer radiation belt computed with the verb code, *J. Geophys. Res.*, *114*, A11209, doi:10.1029/2008JA013784.
- Smith, A. J., R. B. Horne, and N. P. Meredith (2004a), Ground observations of chorus following geomagnetic storms, *J. Geophys. Res.*, *109*, A02205, doi:10.1029/2003JA010204.
- Smith, A. J., N. P. Meredith, and T. P. O'Brien (2004b), Differences in ground-observed chorus in geomagnetic storms with and without enhanced relativistic electron fluxes, *J. Geophys. Res.*, *109*, A11204, doi:10.1029/2004JA010491.
- Smith, A. J., R. B. Horne, and N. P. Meredith (2010), The statistics of natural ELF/VLF waves derived from a long continuous set of ground-based observations at high latitude, *J. Atmos. Sol. Terr. Phys.*, *72*, 463–475, doi:10.1016/j.jastp.2009.12.018.
- Sonwalkar, V. S., and J. Harikumar (2000), An explanation of ground observations of auroral hiss: Role of density depletions and meter-scale irregularities, *J. Geophys. Res.*, *105*, 18,867–18,883, doi:10.1029/1999JA000302.
- Spasojevic, M., and U. S. Inan (2005), Ground based VLF observations near $L = 2.5$ during the Halloween 2003 storm, *Geophys. Res. Lett.*, *32*, L21103, doi:10.1029/2005GL024377.
- Spasojevic, M., and U. S. Inan (2010), Drivers of chorus in the outer dayside magnetosphere, *J. Geophys. Res.*, *115*, A00F09, doi:10.1029/2009JA014452.
- Summers, D., B. Ni, and N. P. Meredith (2007), Timescales for radiation belt electron acceleration and loss due to resonant wave-particle interactions: 2. Evaluation for VLF chorus, ELF hiss, and electromagnetic ion cyclotron waves, *J. Geophys. Res.*, *112*, A04207, doi:10.1029/2006JA011993.
- Thorne, R. M. (2010), Radiation belt dynamics: The importance of wave-particle interactions, *Geophys. Res. Lett.*, *37*, L22107, doi:10.1029/2010GL044990.
- Thorne, R. M., T. P. O'Brien, Y. Y. Shprits, D. Summers, and R. B. Horne (2005), Timescale for mev electron microburst loss during geomagnetic storms, *J. Geophys. Res.*, *110*, A09202, doi:10.1029/2004JA010882.
- Tsuruda, K., S. Machida, T. Terasawa, A. Nishida, and K. Maezawa (1982), High spatial attenuation of the Siple transmitter signal and natural VLF chorus observed at ground-based chain stations near Roberval, Quebec, *J. Geophys. Res.*, *87*, 742–750, doi:10.1029/JA087iA02p00742.
- Tsurutani, B. T., and E. J. Smith (1977), Two types of magnetospheric ELF chorus and their substorm dependences, *J. Geophys. Res.*, *82*, 5112–5128, doi:10.1029/JA082i032p05112.
- Tsyganenko, N. A. (1995), Modeling the Earth's magnetospheric magnetic field confined within a realistic magnetopause, *J. Geophys. Res.*, *100*, 5599–5612, doi:10.1029/94JA03193.
- Tsyganenko, N. A., and M. I. Sitnov (2005), Modeling the dynamics of the inner magnetosphere during strong geomagnetic storms, *J. Geophys. Res.*, *110*, A03208, doi:10.1029/2004JA010798.
- Turner, N. E., W. D. Cramer, S. K. Earles, and B. A. Emery (2009), Geoefficiency and energy partitioning in CIR-driven and CME-driven storms, *J. Atmos. Sol. Terr. Phys.*, *71*, 1023–1031, doi:10.1016/j.jastp.2009.02.005.
- Tverskaya, L. V., N. N. Pavlov, J. B. Blake, R. S. Selesnick, and J. F. Fennell (2003), Predicting the L-position of the storm-injected relativistic electron belt, *Adv. Space Res.*, *31*, 1039–044, doi:10.1016/S0273-1177(02)00785-8.
- Varotsou, A., D. Boscher, S. Bourdarie, R. B. Horne, N. P. Meredith, S. A. Glauert, and R. H. Friedel (2008), Three-dimensional test simulations of the outer radiation belt electron dynamics including electron-chorus resonant interactions, *J. Geophys. Res.*, *113*, A12212, doi:10.1029/2007JA012862.

- Walker, A. D. M. (1974), Excitation of the Earth-ionosphere waveguide by downgoing whistlers. II. Propagation in the magnetic meridian, *Proc. R. Soc. London, Ser. A*, *340*, 375–393, doi:10.1098/rspa.1974.0158.
- Wiltberger, M., R. Lopez, and J. Lyon (2003), Magnetopause erosion: A global view from MHD simulation, *J. Geophys. Res.*, *108*(A6), 1235, doi:10.1029/2002JA009564.
- Yan, X., J. LaBelle, G. Haerendel, M. Spasojevic, N. Bunch, D. I. Golden, H. U. Frey, and A. T. Weatherwax (2013), Dayside auroral hiss observed at South Pole Station, *J. Geophys. Res. Space Physics*, *118*, 1220–1230, doi:10.1002/jgra.50141.
- Zhao, H., and X. Li (2013), Inward shift of outer radiation belt electrons as a function of *Dst* index and the influence of the solar wind on electron injections into the slot region, *J. Geophys. Res. Space Physics*, *118*, 756–764, doi:10.1029/2012JA018179.